An Atomic-Scale Understanding of UO_2 Surface Evolution During Anoxic Dissolution

Aleksej J. Popel[a*], Steven R. Spurgeon[b], Bethany Matthews[b], Matthew J. Olszta[b], Beng Thye Tan[a], Thomas Gouder[c], Rachel Eloirdi[c], Edgar C. Buck[b], Ian Farnan[a]

[a]Department of Earth Sciences, University of Cambridge, Downing Street, Cambridge CB2 3EQ, United Kingdom

[b]Energy and Environment Directorate, Pacific Northwest National Laboratory, Richland, WA, 99352, USA

[c]European Commission, Joint Research Centre, Directorate for Nuclear Safety and Security, Postfach 2340, DE-76215 Karlsruhe, Germany

[*] Corresponding author. E-mail address: apopel@cantab.net (A.J. Popel).

Abstract

Our present understanding of surface dissolution of nuclear fuels such as uranium dioxide (UO_2) is limited by the use of non-local characterization techniques. Here we discuss the use of state-of-the-art scanning transmission electron microscopy (STEM) to reveal atomic–scale changes occurring to a UO_2 thin film subjected to anoxic dissolution in deionised water. No amorphisation of the UO_2 film surface during dissolution is observed, and dissolution occurs preferentially at surface reactive sites that present as surface pits which increase in size as the dissolution proceeds. Using a combination of STEM imaging modes, energy-dispersive X-ray spectroscopy (STEM-EDS), and electron energy loss spectroscopy (STEM-EELS), we investigate structural defects and oxygen passivation of the surface that originates from the filling of the octahedral interstitial site in the centre of the unit cells and its associated lattice contraction. Taken together, our results reveal complex pathways for both the dissolution and infiltration of solutions into UO_2 surfaces.

Keywords: UO_2, TEM, anoxic dissolution, secondary phases, surface oxidation, passivation

1. Introduction

Uranium dioxide (UO_2) is the main form of nuclear fuel used for power generation today.[1] Despite its high practical importance, a mechanistic understanding of UO_2 dissolution is still lacking. This understanding is essential for assessing UO_2 behaviour under various dissolution conditions such as during nuclear fuel failure in water-cooled reactors,[2] subsequent fuel pond storage,[3] and geological disposal.[4, 5] Dissolution, precipitation and passivation of the surface of spent nuclear fuel are important processes that determine the release of uranium and other radionuclides when it is in contact with water. Developing an understanding of surface interactions on UO_2 is the starting point to understand the behaviour of the matrix dissolution of spent nuclear fuel. Sample characterisation techniques commonly reported in the literature for dissolution studies related to nuclear fuel[6-10] are either not surface sensitive, or if they are surface sensitive they sample over large areas. Techniques that provide high-resolution structural information such as crystal truncation rod (CTR) X-ray diffraction (XRD),[11, 12] Raman spectroscopy,[13-17] and X-ray absorption spectroscopy (XAS),[18-20] probe sample volumes several micrometers in size, whereas highly surface sensitive methods such as X-ray photoelectron spectroscopy (XPS)[6, 21-26] probe over areas hundreds of micrometers in lateral and transverse dimensions. Hence, these techniques are challenging to apply to elucidate mechanistic behaviour in atomic-scale dissolution studies. Higher resolution techniques such as transmission electron and scanning electron microscopy (TEM/SEM) have been used to examine secondary phase alteration, colloids, and nanoparticles;[3, 27-32] however, not with modern high resolution instrumentation.

Atomic-resolution TEM has been used to study the evolution of microstructure in nuclear fuel[33-37] and in the assessment of the effect of ion irradiations on UO_2.[38-40]

The key to understanding the long-term rate of release of fission products and actinides from spent nuclear fuel is the rate of dissolution of the UO_2 matrix.[4, 41] This dissolution will be surface-controlled and involve the evolution of the surface and potential new (secondary) phases forming depending on the environment. In our previous work regarding the dissolution of CeO_2 (a non-radioactive analogue of UO_2)[42] and UO_2[43-46] (anoxic conditions) we observed nano-scale surface alteration features and secondary phases that were difficult to identify because of their size.[45, 46] Many unanswered questions surrounding secondary phase formation during anoxic dissolution of UO_2 remain, such as their crystal structure, location, dimensions, and the process by which they form. In addition, it is unclear whether they inhibit the dissolution process and if they support the common assumption that the crystalline actinide dioxides must be covered with an amorphous surface layer as a result of the dissolution.[47-50] In order to address all of these concerns, a high-resolution, sub-micron structural and chemical analysis approach is needed.

In this work we employ state-of-the-art scanning transmission electron microscopy (STEM) to examine the nanoscale evolution of UO_2 crystals during steps in anoxic dissolution. In particular, we use a combination of high-angle annular dark field (STEM-HAADF) and medium-angle annular dark field (STEM-MAADF) imaging, which are sensitive to lattice composition and strain, respectively, as well as high-resolution energy-dispersive X-ray spectroscopy (STEM-EDS) and electron energy loss spectroscopy (STEM-EELS) to examine the local chemical evolution of the

system. For this purpose, a thin film sample of UO_2 subjected to anoxic dissolution in deionised water described in refs 45, 46 was studied to reveal surface alteration features and identify secondary phase formations. The increase in resolution provided by atomic-scale chemical imaging of the dissolution process allows us to examine the extent of the amorphous surface hydroxide phase that is often postulated to mediate dissolution.[47, 49] We find evidence for an alternative passivation mechanism through light element atomic-scale mapping, shedding light on the complex nature of dissolution in this system.

2. Experiment

2.1. Sample Production. The thin film of UO_2 used in this study was produced by reactive magnetron sputtering onto a Si (001) single crystal substrate. The dissolution experiment was performed in a glovebox under argon atmosphere, with oxygen level ≤ 0.1 ppm O_2, in de-aerated deionised water for 140 days and the thin film sample was annealed in Ar/5%H_2 at 800˚C immediately before the leaching experiment. Further details for the leached sample on the sample production, the dissolution experiment, and characterisation by SEM, electron backscatter diffraction (EBSD), and XRD are given in refs 45, 46.

A reference sample for comparison purposes was produced at the same Labstation machine at the JRC Karlsruhe as the leached sample. Following cleaning with ethanol and heating to ~400 °C under pO_2 of 2×10^{-6} mbar for 10 min, the Si substrate was maintained at a temperature of 300–350 °C for the film deposition. A partial pressure of Ar was set to 5×10^{-3} mbar and an O_2 partial pressure was set to

2×10^{-5} mbar. The reference film sample was deposited for a shorter time (10 min versus 30 min) and at a lower target power (1.38 W) than the leached sample (3.2 W), which resulted in a lower film thickness. The reference sample was a nominal thickness of 40 nm, compared to the other sample, which was nominally six times thicker at 240 nm.

2.2. Electron Microscopy. SEM imaging of the sample surface was performed using a FEI Helios NanoLab 660 DualBeam Ga^+ Focused Ion Beam (FIB) microscope, operating at 5 kV accelerating voltage and a current of 0.4 nA. STEM samples were prepared on the same system using a standard lift out procedure. The sample was thinned using a high to low angle procedure while lowering the ion beam accelerating voltage from 30 kV to 5 kV. Final thinning and polishing were performed at 2 kV at an angle of 59°. STEM data were collected on a probe-corrected JEOL ARM-300F microscope operating at 300 kV accelerating voltage, with a probe semi-convergence angle of 29.7 mrad. Simultaneous STEM-HAADF and STEM-MAADF images were collected using collection angles of 72–497 mrad and 47–145 mrad, respectively. Tilt series were acquired in 3° steps in the holder α tilt direction totalling ±15° off the [100] zone axis followed by subsequent rigid-alignment using the Smart Align plugin.[51] EDS and DualEELS maps were collected using a ~1 Å probe size and a ~230 pA probe current, with the latter using a 0.25 eV ch^{-1} energy dispersion. The EELS spectra were corrected for energy drift using simultaneously acquired zero-loss mapping and subsequently denoised using principal component analysis (PCA).

3. Results and Discussion

We first examine the microstructures of both the unleached and leached samples (Figure 1). The thin film used in the dissolution experiment was grown ~6 times thicker than the unleached reference sample (40 nm as compared to 240 nm, Figures 1a and 1c). Both films are comprised of columnar grains on the order of 5-10 nm in lateral dimension that were observed to extend from the Si substrate to the outer surface (Figure 1b). STEM-HAADF imaging confirms the atomic columns of UO_2 (with black arrows indicating grain boundaries). Small, equiaxed grains of a few nm in dimension were also observed near the UO_2/Si substrate, but were only noted at the interface and not throughout the film (Figure 1b). The same columnar grain boundary microstructures are shown in the STEM-HAADF image of the leached sample, Figure 1c, with the grains extending from the Si/UO_2 interface to the leached surface. Cracks in the film are also present throughout.

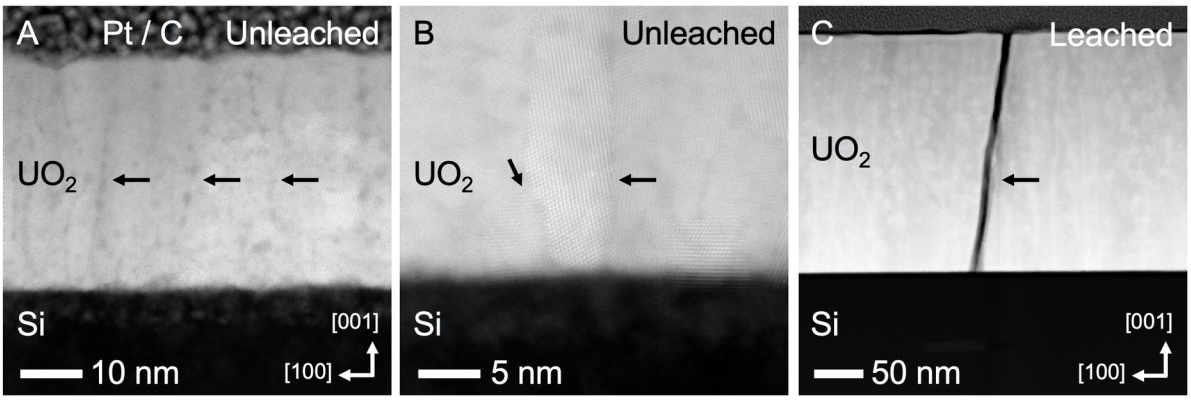

Figure 1. Sample microstructure. (a) Low and (b) high-magnification cross-sectional STEM-HAADF images of the unleached sample, revealing nanoscale grain structures, marked by the black arrows. (c) Cross-sectional STEM-HAADF image of a crack in the leached sample running from surface to substrate, marked with a black arrow.

Closer examination of the surfaces of both the unleached and leached surfaces (Figure 2) reveals shallow pitting associated with grain boundaries intersecting the

surface. The grain boundary in the unleached surface (Figure 2a) is evidenced both by the dark linear contrast (black arrow) as well as the atomic columns of adjacent grains. While the line is offset from the atomic column contrast, this is a function of the boundary inclined within the foil. The dark line appears to align well with contrast at the surface of the sample, thereby suggesting this is a grain boundary and not a dislocation. Regardless, both the STEM-MAADF contrast and the linear contrast appear directly below the surface pit, which is ~ 5 nm wide.

Similar grain boundary contrast was observed in leached sample (Figure 2b). While the appearance of continuous atomic columns is continuous across the two, bright linear grain boundary figures, this is most likely a function of the extremely localized electron STEM probe focusing on a single grain either above or below the two grain boundaries. Provided the grain widths are on the order of 5-10 nm, it would suggest that even for a TEM foil 50-75 nm thick there would be a projection of 5-10 grains in any given projection. Above the two grain boundaries a larger (~50 nm) wide pit was observed, suggesting that the smaller pits in the unleached sample grow as a function of dissolution process. The high density of exposed grain boundaries at the surface likely provide energetically favourable sites for dissolution[52-55] and, hence, the growth of surface pits. The contrast of the Pt/C protective layer deposited during FIB milling is observed within the pits in either image, proving that their appearance or growth is not a sample preparation artefact.

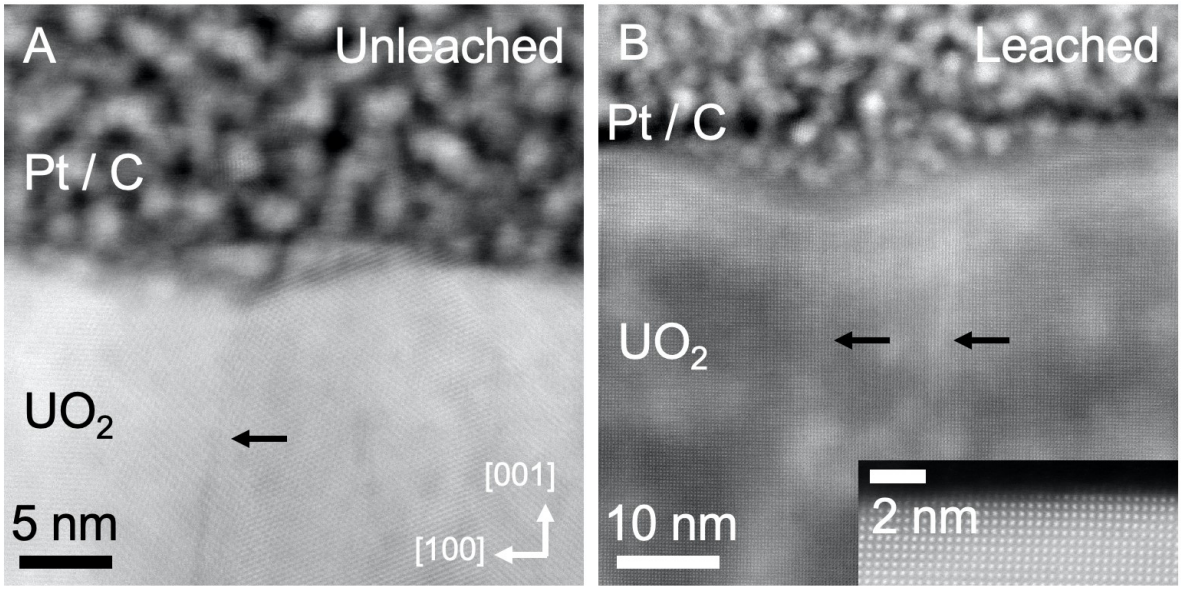

Figure 2. Surface pit formation. Cross-sectional STEM-MAADF images of the unleached (a) and leached (b) samples, confirming that the intersection of nanoscale grains results in pits at the sample surface, marked by the black arrows. The STEM-HAADF inset in (b) shows the detail of another pit, which exhibits crystalline steps all the way to the surface.

The leached sample had been held in deionised water for 140 days prior to imaging, and uranium concentrations had peaked and lowered to a steady state and were in the range $1.1 \times 10^{-9} – 3.0 \times 10^{-9}$ mol/l.[38, 39] For these dissolution conditions the presence of an 'amorphous $U(OH)_4$ phase' on the surface is often inferred from solubility arguments[47, 49] and therefore presumed to control the solubility. We do not observe the formation of this phase as indicated by STEM-HAADF image inset in Figure 2b, although we cannot exclude the presence of U-OH termination of uranium atoms on the surface. This finding is consistent with our earlier observation of the lack of the surface amorphisation by the surface-sensitive EBSD technique in refs 45, 46.

As we have reported previously,[38, 39] the presence of extensive cracking and surface protrusions was also observed. The two heat treatment conditions in this study allow us to examine the possible origin of these cracks, which may be linked to thermal expansion differences between the UO_2 film and Si substrate during cooling or annealing before leaching. While the expected in-plane lattice mismatch for UO_2 and pure Si is low $\left(\frac{a_{UO2}-a_{Si}}{a_{Si}}=\frac{5.47-5.43}{5.43}=0.07\%\right)$, the linear thermal expansion coefficients of the silicon substrate and the UO_2 film differ by a factor of three at the preparation temperature (UO_2 > Si).[56, 57] This difference may well lead to the build-up of local strain and the emergence of novel nanoscale features as the strain state evolves during thermal treatment and subsequent leaching.

Evidence for such novel behaviour is shown in Figure 3a, where SEM secondary electron (SE) imaging reveals extensive cracking and large, faceted bundles on the sample surface that appear to be precipitates. However, cross-sectional STEM analysis of these regions (shown in Figures 3b and 3c and in supplementary movie S1) demonstrate that these are actually regions of buckled UO_2 film. During the leaching process oxygen infiltrates existing cracks and grain boundaries, thereby leading to extensive variations in local strain state. These surface sites may also act as preferential nucleation sites[55] for uranium from the solution that results in swelling and an associated stress. In some regions buckling with detachment from the substrate does occur, resulting in rotation and shear of the nanoscale grain structure, as well as terrace formation on the crystal surface. STEM-EDS mapping (Figures 3d–g) of the buckling confirms its identical composition to the pristine film region and

reveals an increase in oxygen content at the film-substrate interface and sample surface.

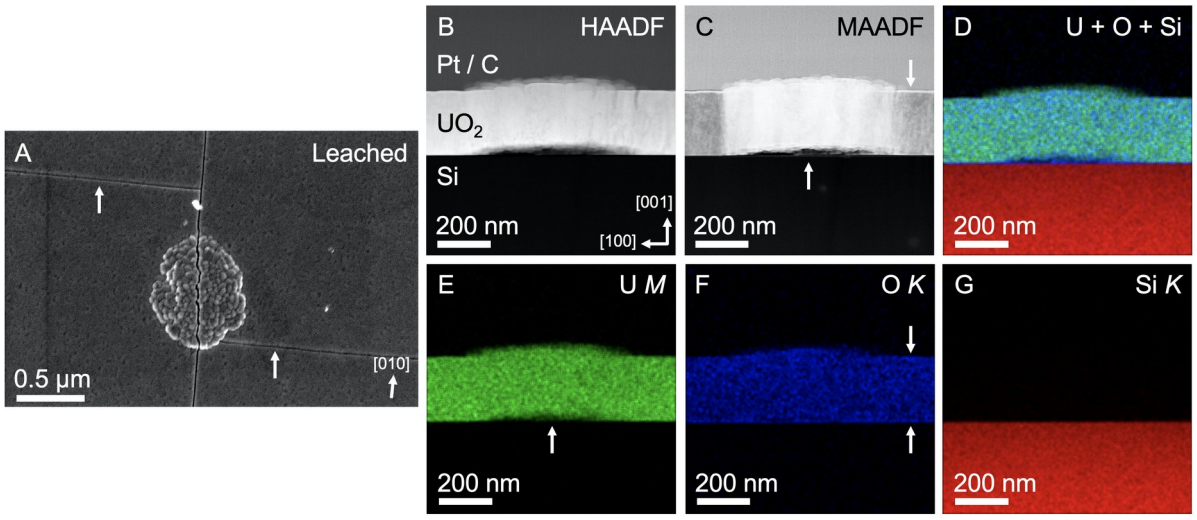

Figure 3. Evidence for film buckling. (a) Representative SE image showing surface cracks (marked by arrows) and a large buckled region of the crystal (center) of the kind from which a lift out was extracted. (b) and (c) Cross-sectional STEM-HAADF and STEM-MAADF images revealing that the film has buckled away from the substrate and sheared into rod-like features. The arrows in C mark the buckling and excess surface oxygen, respectively. (d–g) Combined and individual STEM-EDS maps for the U *M*, O *K*, and Si *K* peaks, respectively. The arrows mark the loss of mass at the buckled region (e) and excess oxygen at both the crystal surface and substrate interface (f).

To further explore the dynamics of the dissolution process, we measure the oxygen content of the film surface and its defects using STEM-EELS, which is highly sensitive to light element composition. As shown in Figures 4a and 4b, the unleached sample shows extensive oxygen build-up at the sample surface. Similar excess oxygen is present in the leached sample, shown in Figures 4c and 4d, but more pronounced. In this case we observe infiltration of excess oxygen into the surface regions of the crack, where it lines a ~5 nm region along the crack and

surface. As the UO_2 thin film was annealed in Ar/5%H_2 at 800˚C immediately before leaching and not exposed to any atmospheric oxygen until being examined by SEM after the experiment, we suggest that this excess oxygen originates at least in part from the dissolution process. In the absence of an oxidising agent in these anoxic conditions and where radiolytic production of oxidising species for this natural uranium sample is insignificant, this process could occur by the reduction of water. The potential–pH diagram showing the relative stabilities of uranium phases (Figure 5 in ref 4) indicates a region between the UO_2/U and H_2O/H_2 equilibrium lines in which going from UO_2 to UO_{2+x} could reduce water at the sample surface. Such a process would be described by the following overall chemical equation that has been proposed before by Haschke et al.[58] for PuO_2 and adsorbed water:

$$UO_2(s) + xH_2O(ads.) \rightarrow UO_{2+x}(s) + 2xH_2(g) \quad (1).$$

Idriss[59] also discussed oxidation of polycrystalline UO_2 with H_2O vapour where the subsurface is oxidized with oxygen diffusion originating from dissociation of H_2O vapour on the surface and noted that this dissociative vapour adsorption is favoured at defective surfaces. This surface reaction is also consistent with the passivation of the dissolution process presented in refs 45, 46 and relevant for the cases when oxidising agents are absent under anoxic conditions and where radiolytic production of oxidising species is insignificant.

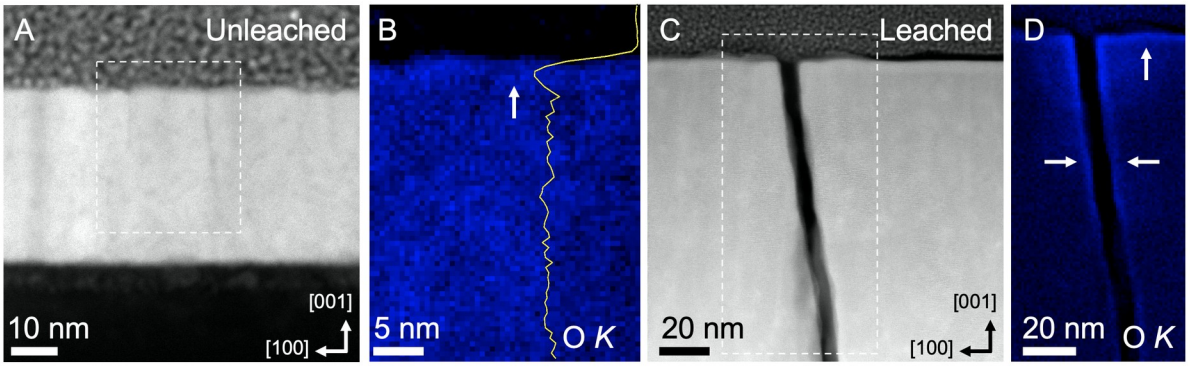

Figure 4. Chemical analysis of excess oxygen. Cross-sectional STEM-HAADF images and corresponding STEM-EELS maps of the O *K* edge from the dashed regions in the unleached (a) and (b) and leached (c) and (d) samples, respectively. Excess oxygen lines the cracks and surface, marked by the arrows and the yellow integrated line profile in (b), respectively.

This observation is consistent with previous literature reports of the dissolution of UO_2 in buffered water (pH 7.3, free from dissolved inorganic carbon) under a reducing atmosphere (5% H_2/95% N_2), where the surface oxidation to 7–10% U(VI) and 20% U(V) was recorded by XPS without detectable U(VI) in the solution by kinetic phosphorescence analyzer (KPA).[6] Maier et al.[10] also observed oxidative passivation of the UO_2 dissolution under exposure to 2.25 mM H_2O_2 solution in de-aerated 10 mM bicarbonate solution. It is known that across the low range of UO_{2+x} oxidation [$x < 0.25$; U_4O_9], where the cubic structure is maintained, the excess oxygen occupies positions ~1 Å from the body centre and the unit cell also experiences a contraction.[12] In addition, Spurgeon et al.[60] observed by STEM-EELS no evidence for large scale phase transformations at a stoichiometry of nearly $UO_{2.67}$ near the surface. We suggest that once the interstitial site is filled and the unit cell is contracted, further oxidation and dissolution are inhibited. This passivation mechanism is similar to the oxidation inhibition mechanisms proposed for trivalent rare earth dopants in UO_2[61, 62] where dopants might result in a reduction in the availability of the interstitial sites and lattice contraction that results in decreased

mobility of the O^{2-} ions into the vacant sites in the fluorite lattice. Since the oxidation reaction involves the incorporation of O^{2-} ions into the fluorite lattice, these effects could be expected to limit the extent of oxygen propagation further into the UO_2 matrix.

4. Conclusions

The application of atomic-scale imaging to the dissolution process of UO_2 reveals that dissolution initiates at surface grain boundaries and film cracks. However, the dissolution process does not result in the formation of a hydrous amorphous $U(OH)_4$ phase. Instead, we suggest a process of oxygen substitution into the central octahedral interstitial site in the surface layers of the UO_2 lattice during dissolution. This appears to create an oxidised passivating layer, which would be responsible for the observed reduction in uranium release as a function of leaching time. The earlier features observed by SEM as secondary phases were confirmed to be UO_2. Our highly local analyses reveal unique pathways for oxygen incorporation into UO_2 surfaces.

Acknowledgments

S.R.S., B.M., M.J.O., and E.C.B. were supported by the Laboratory Directed Research and Development (LDRD) Nuclear Processing Science Initiative (NPSI) at Pacific Northwest National Laboratory (PNNL). PNNL is a multiprogram national laboratory operated for the U.S. Department of Energy (DOE) by Battelle Memorial Institute under Contract No. DE-AC05-76RL0-1830. STEM sample preparation and imaging was performed in the Radiological Microscopy Suite (RMS), located in the Radiochemical Processing Laboratory (RPL) at PNNL.

Supporting Information

Movie S1: Colorized cross-sectional STEM-HAADF tilt series of UO_2 film buckling and shear into rod-like regions. Tilt range = ±15º in 3º steps.

References

1. Wiss, T.; Hiernaut, J.-P.; Roudil, D.; Colle, J.-Y.; Maugeri, E.; Talip, Z.; Janssen, A.; Rondinella, V.; Konings, R. J. M.; Matzke, H.; Weber, W. J., Evolution of spent nuclear fuel in dry storage conditions for millennia and beyond. *J. Nucl. Mater.* **2014,** *451* (1-3), 198-206.

2. Burns, P. C.; Ewing, R. C.; Navrotsky, A., Nuclear Fuel in a Reactor Accident. *Science* **2012,** *335*, 1184-1188.

3. Neill, T.; Morris, K.; Pearce, C. I.; Sherriff, N. K.; Burke, M. G.; Chater, P. A.; Janssen, A.; Natrajan, L.; Shaw, S., Stability, Composition, and Core−Shell Particle Structure of Uranium(IV)-Silicate Colloids. *Environ. Sci. Technol.* **2018,** *52*, 9188-9127.

4. Shoesmith, D. W., Fuel corrosion processes under waste disposal conditions. *J. Nucl. Mater.* **2000,** *282*, 1-31.

5. Ewing, R. C., Long-term storage of spent nuclear fuel. *Nat. Mater.* **2015,** *14* (3), 252-257.

6. Ulrich, K.-U.; Ilton, E. S.; Veeramani, H.; Sharp, J. O.; Bernier-Latmani, R.; Schofield, E. J.; Bargar, J. R.; Giammar, D. E., Comparative dissolution kinetics of biogenic and chemogenic uraninite under oxidizing conditions in the presence of carbonate. *Geochim. Cosmochim. Acta* **2009,** *73* (20), 6065-6083.

7. Casella, A.; Hanson, B.; Miller, W., The effect of fuel chemistry on UO_2 dissolution. *J. Nucl. Mater.* **2016,** *476*, 45-55.

8. Mohun, R.; Desgranges, L.; Canizarès, A.; Raimboux, N.; Duval, F.; Omnee, R.; Jégou, C.; Miro, S.; Simon, P., Investigating the role of irradiation defects during UO_2 oxidative dissolution. *J. Nucl. Mater.* **2018,** *509*, 305-312.

9. Liu, N.; He, H.; Noël, J. J.; Shoesmith, D. W., The Electrochemical Study of Dy_2O_3 Doped UO_2 in Slightly Alkaline Sodium Carbonate/bicarbonate and Phosphate Solutions. *Electrochim. Acta* **2017,** *235*, 654-663.

10. Maier, A. C.; Kegler, P.; Klinkenberg, M.; Baena, A.; Finkeldei, S.; Brandt, F.; Jonsson, M., On the change in UO_2 redox reactivity as a function of H_2O_2 exposure. *Dalton Trans.* **2020,** *49*, 241–1248.

11. Stubbs, J. E.; Chaka, A. M.; Ilton, E. S.; Biwer, C. A.; Engelhard, M. H.; Bargar, J. R.; Eng, P. J., UO_2 Oxidative Corrosion by Nonclassical Diffusion. *Phys. Rev. Lett.* **2015,** *114* (24), 246103.

12. Stubbs, J. E.; Biwer, C. A.; Chaka, A. M.; Ilton, E. S.; Du, Y.; Bargar, J. R.; Eng, P. J., Oxidative Corrosion of the UO_2 (001) Surface by Nonclassical Diffusion. *Langmuir* **2017,** *33* (46), 13189-13196.

13. Jégou, C.; Caraballo, R.; De Bonfils, J.; Broudic, V.; Peuget, S.; Vercouter, T.; Roudil, D., Oxidizing dissolution of spent MOX47 fuel subjected to water radiolysis: Solution chemistry and surface characterization by Raman spectroscopy. *J. Nucl. Mater.* **2010,** *399* (1), 68-80.

14. Elorrieta, J. M.; Bonales, L. J.; Rodriguez-Villagra, N.; Baonza, V. G.; Cobos, J., A detailed Raman and X-ray study of UO_{2+x} oxides and related structure transitions. *Phys. Chem. Chem. Phys.* **2016,** *18* (40), 28209-28216.

15. Palacios, M. L.; Taylor, S. H., Characterization of uranium oxides using *in situ* micro-Raman spectroscopy. *Appl. Spectrosc.* **2000,** *54* (9), 1372-1378.

16. Desgranges, L.; Baldinozzi, G.; Simon, P.; Guimbretière, G.; Canizares, A., Raman spectrum of U_4O_9: a new interpretation of damage lines in UO_2. *J. Raman Spectrosc.* **2012,** *43* (3), 455-458.

17. Guimbretière, G.; Desgranges, L.; Canizarès, A.; Carlot, G.; Caraballo, R.; Jégou, C.; Duval, F.; Raimboux, N.; Ammar, M. R.; Simon, P., Determination of in-depth damaged profile by Raman line scan in a pre-cut He^{2+} irradiated UO_2. *Appl. Phys. Lett.* **2012,** *100* (25).

18. Conradson, S. D.; Manara, D.; Wastin, F.; Clark, D. L.; Lander, G. H.; Morales, L. A.; Rebizant, J.; Rondinella, V. V., Local Structure and Charge Distribution in the UO_2−U_4O_9 System. *Inorg. Chem.* **2004,** *43*, 6922−6935.

19. Butorin, S. M.; Modin, A.; Vegelius, J. R.; Kvashnina, K. O.; Shuh, D. K., Probing Chemical Bonding in Uranium Dioxide by Means of High-Resolution X-ray Absorption Spectroscopy. *J. Phys. Chem. C* **2016,** *120* (51), 29397-29404.

20. Leinders, G.; Bes, R.; Kvashnina, K. O.; Verwerft, M., Local Structure in U(IV) and U(V) Environments: The Case of U_3O_7. *Inorg. Chem.* **2020,** *59* (7), 4576-4587.

21. Sunder, S.; Shoesmith, D. W.; Miller, N. H., Oxidation and dissolution of nuclear fuel (UO_2) by the products of the alpha radiolysis of water. *J. Nucl. Mater.* **1997,** *244*, 66-74.

22. Teterin, Y. A.; Kulakov, V. M.; Baev, A. S.; Nevzorov, N. B.; Melnikov, I. V.; Streltsov, V. A.; Mashirov, L. G.; Suglobov, D. N.; Zelenkov, A. G., A study of synthetic and natural uranium oxides by X-ray photoelectron spectroscopy. *Phys. Chem. Minerals* **1981,** *7* (4), 151-158.

23. Ilton, E. S.; Bagus, P. S., XPS determination of uranium oxidation states. *Surf. Interface Anal.* **2011,** *43* (13), 1549-1560.

24. Ilton, E. S.; Du, Y.; Stubbs, J. E.; Eng, P. J.; Chaka, A. M.; Bargar, J. R.; Nelin, C. J.; Bagus, P. S., Quantifying small changes in uranium oxidation states

using XPS of a shallow core level. *Phys. Chem. Chem. Phys.* **2017,** *19* (45), 30473-30480.

25. de Pablo, J.; Casas, I.; Giménez, J.; Martí, V.; Torrero, M. E., Solid surface evolution model to predict uranium release from unirradiated UO_2 and nuclear spent fuel dissolution under oxidizing conditions. *J. Nucl. Mater.* **1996,** *232*, 138-145.

26. Shoesmith, D. W.; Sunder, S.; Bailey, M. G.; Wallace, G. J., The Corrosion of Nuclear Fuel (UO_2) in Oxygenated Solutions. *Corros. Sci.* **1989,** *29*, 1115-1128.

27. Yan, Q.; Mao, Y.; Zhou, X.; Liang, J.; Ye, M.; Peng, S., Synthesis of UO_2 nanocrystals with good oxidation resistance in water at room temperature. *J. Nucl. Mater.* **2018,** *512*, 417-422.

28. Plakhova, T. V.; Romanchuk, A. Y.; Yakunin, S. N.; Dumas, T.; Demir, S.; Wang, S.; Minasian, S. G.; Shuh, D. K.; Tyliszczak, T.; Shiryaev, A. A.; Egorov, A. V.; Ivanov, V. K.; Kalmykov, S. N., Solubility of Nanocrystalline Cerium Dioxide: Experimental Data and Thermodynamic Modeling. *J. Phys. Chem. C* **2016,** *120* (39), 22615-22626.

29. Kaminski, M. D.; Dimitrijevic, N. M.; Mertz, C. J.; Goldberg, M. M., Colloids from the aqueous corrosion of uranium nuclear fuel. *J. Nucl. Mater.* **2005,** *347*, 77-87.

30. Finn, P. A.; Buck, E. C.; Gong, M.; Hoh, J. C.; Emery, J. W.; Hafenrichter, L. D.; Bates, J. K., Colloidal Products and Actinide Species in Leachate from Spent Nuclear Fuel. *Radiochim. Acta* **1994,** *66/67*, 189-195.

31. Buck, E. C.; Finn, P. A.; Bates, J. K., Electron energy-loss spectroscopy of anomalous plutonium behavior in nuclear waste materials. *Micron* **2004,** *35* (4), 235-243.

32. Wronkiewicz, D. J.; Buck, E., Uranium mineralogy and the geologic disposal of spent nuclear fuel. *Rev. Mineral. Geochem.* **1999,** *38* (1), 475–497.

33. Matzke, H.; Spino, J., Formation of the rim structure in high burnup fuel. *J. Nucl. Mater.* **1997,** *248*, 170-179.

34. Matzke, H.; Blank, H.; Coquerelle, M.; Lassmann, K.; Ray, I. L. F.; Ronchi, C.; Walker, C. T., Oxide fuel transients. *J. Nucl. Mater.* **1989,** *166* (1-2), 165-178.

35. Rondinella, V. V.; Wiss, T., The high burn-up structure in nuclear fuel. *Mater. Today* **2010,** *13* (12), 24-32.

36. Lach, T. G.; Edwards, D. J.; Buck, E. C.; McNamara, B. K.; Schwantes, J. M.; Clark, R. A., Fission recoil-induced microstructural evolution of the fuel-cladding interface [FCI] in high burnup BWR fuel. *J. Nucl. Mater.* **2019,** *521*, 120-125.

37. Wiss, T.; Thiele, H.; Janssen, A.; Papaioannou, D.; Rondinella, V. V.; Konings, R. J. M., Recent Results of Microstructural Characterization of Irradiated Light Water Reactor Fuels using Scanning and Transmission Electron Microscopy. *JOM* **2012,** *64* (12), 1390-1395.

38. Sonoda, T.; Kinoshita, M.; Ishikawa, N.; Sataka, M.; Iwase, A.; Yasunaga, K., Clarification of high density electronic excitation effects on the microstructural evolution in UO_2. *Nucl. Instr. Meth. Phys. Res. B* **2010,** *268* (19), 3277-3281.

39. Wiss, T.; Matzke, H.; Trautmann, C.; Toulemonde, M.; Klaumünzer, S., Radiation damage in UO_2 by swift heavy ions. *Nucl. Instr. Meth. Phys. Res. B* **1997,** *122*, 583-588.

40. Matzke, H.; Lucuta, P. G.; Wiss, T., Swift heavy ion and fission damage effects in UO_2. *Nucl. Instr. Meth. Phys. Res. B* **2000,** *166-167*, 920-926.

41. Shoesmith, D. W.; Sunder, S., The prediction of nuclear fuel (UO_2) dissolution rates under waste disposal conditions. *J. Nucl. Mater.* **1992,** *190*, 20-35.

42. Popel, A. J.; Le Solliec, S.; Lampronti, G. I.; Day, J.; Petrov, P. K.; Farnan, I., The effect of fission-energy Xe ion irradiation on the structural integrity and dissolution of the CeO_2 matrix. *J. Nucl. Mater.* **2017,** *484*, 332-338.

43. Popel, A. J.; Petrov, V. G.; Lebedev, V. A.; Day, J.; Kalmykov, S. N.; Springell, R.; Scott, T. B.; Farnan, I., The effect of fission-energy Xe ion irradiation on dissolution of UO_2 thin films. *J. Alloys Compd.* **2017,** *721*, 586-592.

44. Popel, A. J.; Wietsma, T. W.; Engelhard, M. H.; Lea, A. S.; Qafoku, O.; Grygiel, C.; Monnet, I.; Ilton, E. S.; Bowden, M. E.; Farnan, I., The effect of ion irradiation on the dissolution of UO_2 and UO_2-based simulant fuel. *J. Alloys Compd.* **2018,** *735*, 1350-1356.

45. Tan, B. T.; Popel, A. J.; Wilbraham, R. J.; Day, J.; Lampronti, G. I.; Boxall, C.; Farnan, I., Surface and electrochemical controls on UO_2 dissolution under anoxic conditions. *J. Nucl. Mater.* **2019,** *520*, 41-55.

46. Popel, A. J.; Tan, B. T.; Gouder, T.; Lampronti, G. I.; Day, J.; Eloirdi, R.; Seibert, A.; Farnan, I., Surface alteration evidence for a mechanism of anoxic dissolution of UO_2. *Appl. Surf. Sci.* **2019,** *464*, 376-379.

47. Neck, V.; Kim, J. I., Solubility and hydrolysis of tetravalent actinides. *Radiochim. Acta* **2001,** *89*, 1-16.

48. Kim, S. S.; Baik, M. H.; Kang, K. C.; Choi, J. W., Comparison between experimentally measured and thermodynamically calculated solubilities of UO_2 and ThO_2 in KURT ground water. *Nucl. Eng. Technol.* **2009,** *41*, 867-874.

49. Fanghänel, T.; Neck, V., Aquatic chemistry and solubility phenomena of actinide oxides/hydroxides. *Pure Appl. Chem.* **2002,** *74*, 1895-1907.

50. Vitorge, P.; Capdevila, H.; Maillard, S.; Faure, M.-H.; Vercouter, T., Thermodynamic stabilities of MO_{2+x}(s) (M = U, Np, Pu and Am), Pourbaix diagrams. *J. Nucl. Sci. Technol.* **2002,** *39* (3), 713-716.

51. Jones, L.; Yang, H.; Pennycook, T. J.; Marshall, M. S. J.; Van Aert, S.; Browning, N. D.; Castell, M. R.; Nellist, P. D., Smart Align—a new tool for robust non-rigid registration of scanning microscope data. *Adv. Struct. Chem. Imaging* **2015,** *1* (1).

52. Schwertmann, U., Solubility and dissolution of iron oxides. *Plant Soil* **1991,** *130*, 1-25.

53. Corkhill, C. L.; Myllykyla, E.; Bailey, D. J.; Thornber, S. M.; Qi, J.; Maldonado, P.; Stennett, M. C.; Hamilton, A.; Hyatt, N. C., Contribution of energetically reactive surface features to the dissolution of CeO_2 and ThO_2 analogues for spent nuclear fuel microstructures. *ACS Appl. Mater. Interfaces* **2014,** *6* (15), 12279-12289.

54. Corkhill, C. L.; Bailey, D. J.; Tocino, F. Y.; Stennett, M. C.; Miller, J. A.; Provis, J. L.; Travis, K. P.; Hyatt, N. C., Role of Microstructure and Surface Defects on the Dissolution Kinetics of CeO_2, a UO_2 Fuel Analogue. *ACS Appl. Mater. Interfaces* **2016,** *8* (16), 10562-10571.

55. Stumm, W., Reactivity at the mineral-water interface: dissolution and inhibition. *Colloids Surf. A Physicochem. Eng. Asp.* **1997,** *120*, 143-166.

56. Nelson, A. T.; Rittman, D. R.; White, J. T.; Dunwoody, J. T.; Kato, M.; McClellan, K. J.; White, A. M., An Evaluation of the Thermophysical Properties of Stoichiometric CeO_2 in Comparison to UO_2 and PuO_2. *J. Am. Ceram. Soc.* **2014,** *97* (11), 3652-3659.

57. Okada, Y.; Tokumaru, Y., Precise determination of lattice parameter and thermal expansion coefficient of silicon between 300 and 1500 K. *J. Appl. Phys.* **1984,** *56* (2), 314-320.

58. Haschke, J. M.; Allen, T. H.; Morales, L. A., Reaction of Plutonium Dioxide with Water: Formation and Properties of PuO_{2+x}. *Science* **2000,** *287* (5451), 285-287.

59. Idriss, H., Surface reactions of uranium oxide powder, thin films and single crystals. *Surf. Sci. Rep.* **2010,** *65* (3), 67-109.

60. Spurgeon, S. R.; Sassi, M.; Ophus, C.; Stubbs, J. E.; Ilton, E. S.; Buck, E. C., Nanoscale oxygen defect gradients in UO_{2+x} surfaces. *Proc. Natl. Acad. Sci. U.S.A.* **2019,** *116*, 17181–17186.

61. McEachern, R. J.; Taylor, P., A review of the oxidation of uranium dioxide at temperatures below 400 ^{o}C. *J. Nucl. Mater.* **1998,** *254*, 87-121.

62. Razdan, M.; Shoesmith, D. W., Influence of Trivalent-Dopants on the Structural and Electrochemical Properties of Uranium Dioxide (UO_2). *J. Electrochem. Soc.* **2014,** *161* (3), H105-H113.

Table of Contents

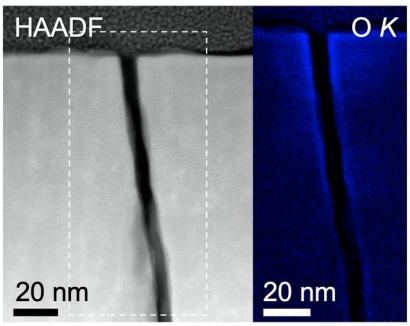

For Table of Contents Only